



Viscophobic turning dictates microalgae transport in viscosity gradients

Michael R. Stehnach[®] ^{1,3}, Nicolas Waisbord^{1,3}, Derek M. Walkama^{1,2} and Jeffrey S. Guasto [®] ¹

Gradients in fluid viscosity characterize microbiomes ranging from mucus layers on marine organisms1 and human viscera^{2,3} to biofilms⁴. Although such environments are widely recognized for their protective effects against pathogens and their ability to influence cell motility2,5, the physical mechanisms regulating cell transport in viscosity gradients remain elusive⁶⁻⁸, primarily due to a lack of quantitative observations. Through microfluidic experiments, we directly observe the transport of model biflagellated microalgae (Chlamydomonas reinhardtii) in controlled viscosity gradients. We show that despite their locally reduced swimming speed, the expected cell accumulation in the viscous region9,10 is stifled by a viscophobic turning motility. This deterministic cell rotationconsistent with a flagellar thrust imbalance 11,12-reorients the swimmers down the gradient, causing their accumulation in the low-viscosity zones for sufficiently strong gradients. Corroborated by Langevin simulations and a three-point force model of cell propulsion, our results illustrate how the competition between viscophobic turning and viscous slowdown ultimately dictates the fate of population-scale microbial transport in viscosity gradients.

Microbial transport is driven by external cues^{5,13} and plays a crucial role in regulating the function of ecosystems ranging from cell colonies4 to Earth's biome14. Swimming microorganisms navigate towards regions of optimal nutrient uptake and photosynthetic productivity by sensing gradients in chemical concentration (that is, chemotaxis^{3,15}) and light intensity (phototaxis¹⁶), respectively. External forces or torques acting on cells can also mechanically guide microbes towards favourable conditions: gravitational fields orient eukaryotic marine microbes within the water column through gravitaxis^{17,18}, and magnetic fields serve as a compass for bacteria in sedimentary environments via magnetotaxis¹⁹. Swimming cells are also widely known to respond to gradients in fluid viscosity⁵, which can vary broadly in scale and strength^{20,21}. Mucus layers (~1 mm thick^{22,23}) exhibit viscosities as low as $2 \text{ cP} (1 \text{ cP} = 10^{-3} \text{ Pa s})$ in corals and sessile marine organisms²⁴, whereas in mammals they can range from 5 cP in the trachea to >1,000 cP in the gastrointestinal tract²¹. Viscous mucus serves as the first line of defence against motile pathogenic bacteria in humans^{2,25} and other organisms¹, and it sustains endangered corals by trapping and distributing microorganisms and nutrient particles1. Despite the far-reaching importance of these systems, a definitive paradigm for swimming cell transport in viscosity gradients is yet to be established, and the physical mechanisms controlling viscotactic motility remain unresolved.

Contrary to the widely studied effects of elevated homogeneous viscosity on cell motility^{26,27}, experimental observations of swimming cell transport in inhomogeneous viscous environments are lacking and largely inconclusive. In viscosity gradients of

unspecified strength, qualitative observations of cell density showed positive^{6,7} and negative⁸ (that is, viscophobic) viscotaxis towards high-and low-viscosity regions, respectively. Recent theoretical and numerical work on swimmer hydrodynamics^{11,12,28} suggests that tuning the cell propulsive apparatus or body asymmetry could produce swimming either up or down the gradient. Although these early experiments and deterministic simulations have provided some insights, the stochastic nature of cell motility and accumulation mechanisms rooted in local swimming speed modulation were largely neglected^{9,10}. A holistic understanding of cell transport in viscosity gradients and the potential mechanisms underlying viscotactic motility has been hampered by a dearth of direct quantitative experiments.

In this Letter, we provide direct evidence of viscophobic motility for the model biflagellated microalga Chlamydomonas reinhardtii^{29,30} (Fig. 1a), which is achieved through a comprehensive experimental description of its transport in a prescribed microfluidic viscosity gradient (Fig. 1b). Our experiments show that as the magnitude of the gradient is increased, a muted cell accumulation in the high-viscosity region⁹ (Fig. 1c,d) gives way to strong accumulation in the low-viscosity region (Fig. 1e). Analysis of cell trajectories and complementary Langevin simulations reveal that this surprising transport behaviour results from the competition between viscous accumulation due to reduced swimming speed9,10 and a viscophobic reorientation mechanism. The latter is consistent with a physical hydrodynamic phenomenon¹², which results in an ensemble drift of swimming C. reinhardtii down the viscosity gradient. Viscophobic reorientation dynamics bear striking similarities to a range of other taxes18,19 and add to the rich diversity of microbial transport mechanisms that regulate important macroscopic ecological processes1-4,13.

To explain the observed migratory behaviour of *C. reinhardtii*, microfluidic devices were designed to precisely control the viscosity gradient over length scales relevant to the swimming cells (Fig. 1b). Briefly, three solutions including a Newtonian viscous polymer solution (polyethylene oxide, PEO), a dilute suspension of C. reinhardtii and cell media were stratified by continuous injection into the microchannel test section (Fig. 1b and Methods). When the flow was stopped, the polymer diffused across the strata for 30 min to form a smooth viscosity profile (Extended Data Fig. 1); thus providing ample time for swimming cells to disperse across the channel. Observations were performed between 30 and 90 min, during which time the viscosity profile, $\eta(x)$, quantified by microrheology, was quasi-steady (Fig. 1g, Extended Data Fig. 2, Extended Data Table 1 and Methods). In the absence of a viscosity gradient, their random walk motility yielded a uniform cell density, ρ , across the channel $(\nabla \eta = 0 \text{ cP} \mu\text{m}^{-1}; \text{ Fig. 1i, Extended Data Fig. 3 and Supplementary})$ Video 1), apart from minor accumulation at the boundaries due to the nature of cell-surface interactions³¹ (Supplementary Section 5.1.2).

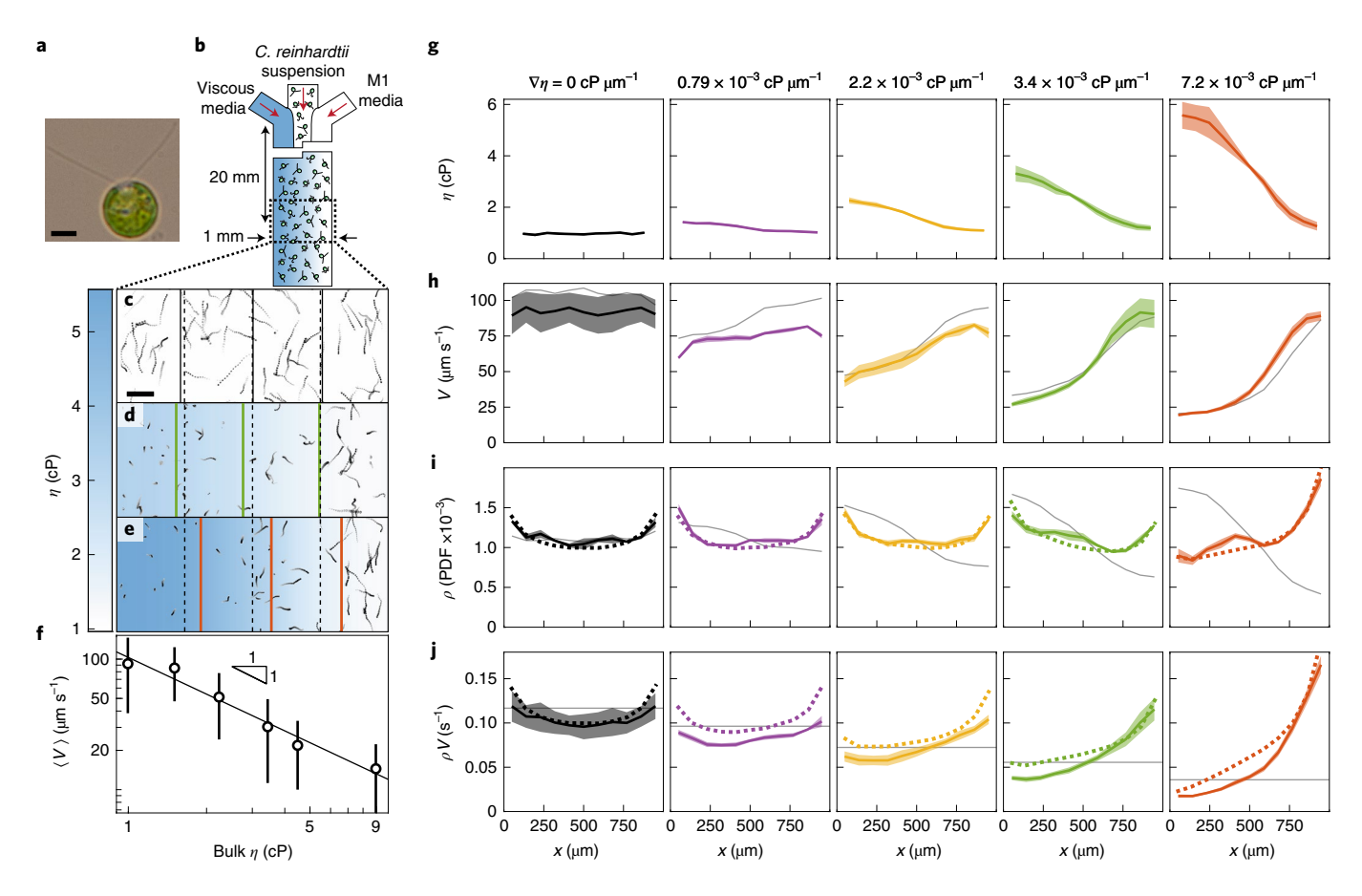


Fig. 1 | Viscosity gradient strength regulates dispersal of swimming microalgae. a, Biflagellated swimming microalga *C. reinhardtii* (wild type). Scale bar, 5 μm. **b**, Schematic of the three-inlet microfluidic device for viscosity gradient generation (100 μm deep). The viscous media (PEO in M1 media), *C. reinhardtii* suspension and M1 media were initially flow-stratified (Methods), then the viscosity gradient formed by polymer diffusion when the flow was stopped (Extended Data Fig. 1). **c-e**, Multi-exposure images (1s duration; intensity increases with time; 60 min post flow) of *C. reinhardtii* show a homogeneous distribution in uniform viscosity (**c**; $\nabla \eta = 0$ cP μm⁻¹, control), slight accumulation in the high-viscosity zone for moderate viscosity gradients (**d**; $\nabla \eta = 3.4 \times 10^{-3}$ cP μm⁻¹) and accumulation in the low-viscosity zone for large gradients (**e**; $\nabla \eta = 7.2 \times 10^{-3}$ cP μm⁻¹). Dashed black lines mark 25%, 50% and 75% of the channel width, and solid lines are the quartiles of cell density in **i**. The colour scale is the measured viscosity profile from **g**. Scale bar, 100 μm. **f**, Ensemble-averaged cell swimming speed, $\langle V \rangle$, in media with bulk viscosity $\eta \sim 2,700$ trajectories each; Supplementary Section 3.1). Error bars show the mean standard deviation (N = 2 - 3) and the black line is a power-law fit²⁶ ($\propto \eta^{-0.93}$). **g**, Microfluidic viscosity profiles measured by microrheology (Methods) and characterized by $\nabla \eta$ (Extended Data Fig. 1 and Extended Data Table 1). The shaded area is the standard deviation (30–90 min post flow). **h-j**, Measured profiles (solid coloured curves) of the local mean cell swimming speed (**h**), cell density (**i**; PDF, probability density function) and flux magnitude (**j**) corresponding to **g**. Shaded regions indicate standard errors (N = 3 - 4 with $\sim 2,100 - 9,200$ trajectories each). The dashed curves are Langevin simulations with viscophobic turning (Fig. 3). Grey curves are analytical predictions for random walk swimmers⁹ without viscoph

For a directionally unbiased random walk, cell density is well known to scale inversely with local swimming speed 9,10,32, $\rho(x) \propto 1/V(x)$. Imposing a moderate viscosity $(\nabla \eta = 3.4 \times 10^{-3} \text{ cP} \, \mu\text{m}^{-1})$ results in a slight accumulation of cells (Fig. 1i, solid coloured lines) in the high-viscosity region that is incommensurate with the strong local reduction in swimming speed (Fig. 1h, coloured lines). The swimming speed distribution quantitatively agrees with analytical predictions (Fig. 1h, grey lines) based on the measured swimming speed of C. reinhardtii in homogeneous conditions²⁶ (Fig. 1f, Extended Data Fig. 4 and Extended Data Table 2) and the independently measured viscosity profile (Fig. 1g and Supplementary Section 4.1). However, this analytical prediction for the slowdown accumulation largely overestimates^{9,10} the observed weakly positive viscotactic behaviour (Fig. 1i, grey line). Stronger gradients reveal a counterintuitive viscophobic regime, where cells accumulate in the low-viscosity region (Fig. 1i, $\nabla \eta = 7.2 \times 10^{-3} \text{ cP} \, \mu\text{m}^{-1}$; Supplementary Video 2). Moreover, the

local cell flux magnitude, $\rho(x)V(x)$, is expected to be spatially uniform across the channel for an unbiased random walk (Fig. 1j, grey lines). As $\nabla \eta$ increases, the progressive deviation of the measured flux magnitude (Fig. 1j, coloured solid lines; Supplementary Section 4.1) from the predicted uniform value is a clear indication of an underlying viscophobic motility bias. To unravel these population-scale observations and determine the nature of the observed behaviour, we examine the kinematics of single-cell motility in the viscosity gradients.

Cells swimming in a viscosity gradient exhibit directional dependence on their rotational kinematics and ultimately reorient down the viscosity gradient. In the absence of a viscosity gradient, cells generally maintain their initial swimming direction for several seconds (Fig. 2a). Conversely, cell trajectories initially oriented at angle, θ , perpendicular to the gradient ($\theta = \pm \pi/2$) continuously bend towards the low-viscosity region ($\theta = 0$; Fig. 2b). This effect is made more apparent by examining the mean cell trajectory (Fig. 2b,

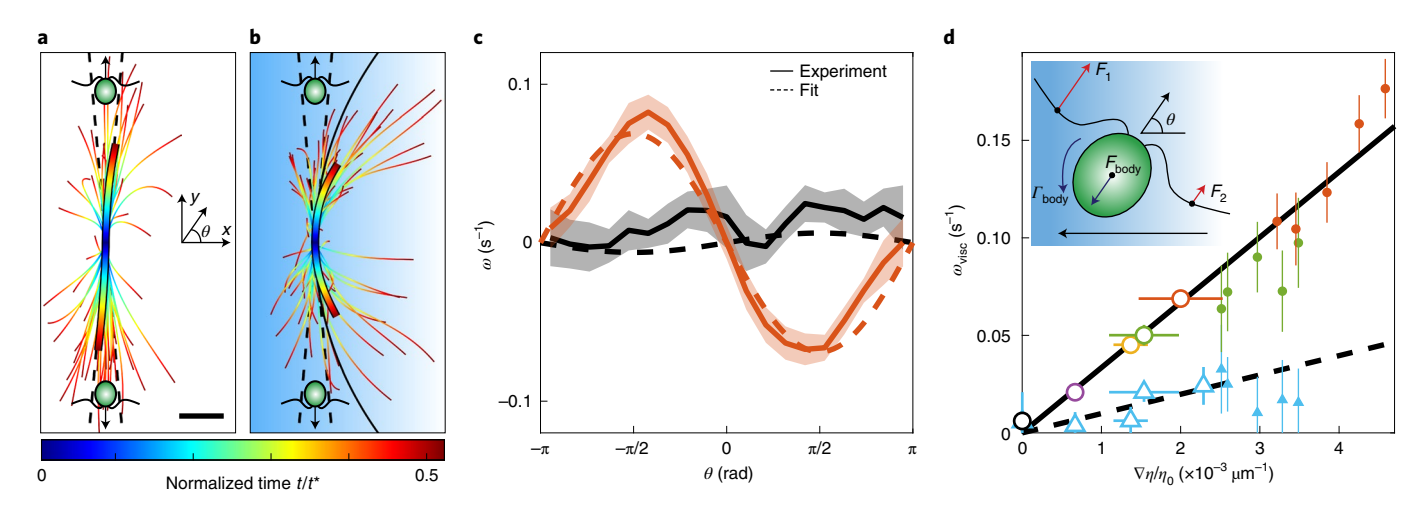


Fig. 2 | Coupling of swimming kinematics to viscosity gradient induces viscophobic turning. a,b, Measured cell trajectories of wild-type *C. reinhardtii* for the control (**a**; $\nabla \eta = 0$ cP μm⁻¹; 65 trajectories) and maximum (**b**; $\nabla \eta = 7.2 \times 10^{-3}$ cP μm⁻¹; 76 trajectories) viscosity gradients. Conditionally sampled from $400 \le x \le 600$ μm and perpendicular to viscosity gradient ($|\theta| = \pi/2 \pm 5^{\circ}$, dashed lines). The thick coloured curves are the mean trajectories, and the black curve in **b** is the analytical prediction (Supplementary Section 4.3). The background shading qualitatively indicates $\nabla \eta$, and $t^* = 500$ μm(V(x))⁻¹ is the characteristic swimming time in the channel. Scale bar, $100 \, \mu$ m. **c**, The angular cell velocity exhibits orientation dependence in a viscosity gradient ($\nabla \eta = 7.2 \times 10^{-3}$ cP μm⁻¹, orange) compared with the control ($\nabla \eta = 0$ cP μm⁻¹, black). Dashed lines are sinusoidal fits, and the shaded regions are standard errors (7,730 and 3,454 trajectories for pooled replicates for black and orange, respectively). **d**, ω_{visc} increases with the normalized viscosity gradient $\nabla \eta / \eta_0$. Wild-type cells (open coloured circles correspond to experiments in Fig. 1g-j; 3,454-7,730 trajectories each) exhibit stronger viscophobic turning compared with short-flagella mutants (open triangles; 792-3,859 trajectories each) in quasi-steady conditions (30-90 min post flow). Solid and dashed black lines are linear fits to open circles and open triangles, respectively. Filled markers correspond to strong gradients sampled from transient viscosity profiles at early times (5-25 min post flow; 319-760 trajectories each; see also Extended Data Fig. 1 and Extended Data Table 3). The filled blue triangles are transient times corresponding to $\nabla \eta = 3.4 \times 10^{-3}$ cP μm⁻¹ quasi-steady experiments. Horizontal error bars stem from the measured viscosity profile, and vertical error bars (obscured by markers) are from the fit in **c**. Inset: potential mechanism for orientation-de

thick coloured curve): owing to the stochastic nature of microbial motility, for example stemming from noise in flagellar actuation and thermal fluctuations^{33,34} (persistence time $\tau_p = 1/2D_r = 7.2 \, \mathrm{s}$ where D_r is the rotational diffusion coefficient; Extended Data Fig. 5 and Methods), a large number of observations are necessary to unveil the underlying deterministic dynamics. Considering all swimming directions, the cells' instantaneous angular velocity displays a sinusoidal dependence on orientation, which is absent from control experiments (Fig. 2c). We hypothesize that viscophobic turning in *C. reinhardtii* results from a slight viscosity difference experienced by its two flagella, causing an imbalance of their drag-based thrust forces³⁵ (inset in Fig. 2d).

A three-point force swimmer model (Supplementary Section 4.2) quantitatively predicts the sinusoidal form of the observed cell rotation rate (dashed curves in Fig. 2c) and captures the mean swimming trajectory of the cells (black curve in Fig. 2b). The angular cell velocity ω is well fitted by the model prediction (Fig. 2c, dashed curves), $\omega(\theta) = -\omega_{\text{visc}} \sin(\theta)$, and quantifies the turning rate amplitude, $\omega_{\rm visc}$. The amplitude grows continuously with the normalized viscosity gradient, $\nabla \eta / \eta_0$, where η_0 is the viscosity in the channel centre, and the largest measured quasi-steady gradient yields a turning time, $\tau = 1/\omega_{\rm visc} \approx 14$ s (Fig. 2d). Furthermore, the linear dependence¹² on $\nabla \eta/\eta_0$ (Fig. 2d, black line) stems from the growth of the turning rate with $\nabla \eta$, which is tempered by enhanced rotational drag through increasing η_0 . A fit of the model prediction (Fig. 2d, black line; Supplementary Section 5.2) $\omega_{\text{visc}} = (V^*/2) \nabla \eta / \eta_0$ gives $V^* \approx 66 \,\mu\text{m s}^{-1}$, which is comparable to the swimming speed of C. reinhardtii in the tested gradients. The cell turning dynamics were also examined during early times in the viscotaxis assay (5-25 min post flow; Extended Data Table 3), when the viscosity gradient was rapidly evolving (Fig. 2d, filled circles). This analysis revealed that the linear increase in $\omega_{\rm visc}$ persists at much higher gradients and emphasized that $\nabla \eta/\eta_0$ controls the growth. Viscophobic reorientation of *C. reinhardtii* seems to be deterministic and omnipresent in viscosity gradients, but the magnitude and nature of the response is also expected to be a strong function of swimmer morphology.

For biflagellated C. reinhardtii, the viscophobic turning rate amplitude decreases with flagellar length. A viscophobic aligning torque is generated by an imbalance in flagellar thrust, whose location, d, is a fraction of the flagellar length, ℓ . To illustrate the dependence on flagellar length, $\omega_{\rm visc}$ was measured for C. reinhardtii mutants whose flagella are 36% shorter than wild-type cells³⁶. The short-flagella cells (Fig. 2d, triangles) exhibit an approximately linear increase in ω_{visc} that is substantially diminished by a factor of 3.3 compared with wild-type cells. Beyond other recent theoretical developments11,12 (Fig. 2d, dashed black line), our three-point force model predicts that flagellar length also determines whether the viscotactic response is negative or positive. The viscophobic aligning torque due to the flagellar thrust imbalance competes with an opposing torque due to a drag imbalance on the spheroidal cell body (that is, translational-rotational coupling³⁷). Biflagellates are thus predicted to behave in a viscophobic manner, when the lateral flagellar centre of thrust is sufficiently large, $d/R > 1/\sqrt{3} \approx 0.577$, compared with the cell body radius, R. Conservatively, taking²⁹ $R \approx 5 \,\mu\text{m}$ and $d \approx \ell/2$, both wild-type cells $(d/R \approx 1.1)$ and short-flagella mutants $(d/R \approx 0.7)$ are expected to exhibit negative viscotaxis, exemplified by our experiments (Fig. 2d). The strong agreement between our measurements and our predictive model, and the consistency with other recent models11,12, points towards a hydrodynamic origin for viscotaxis.

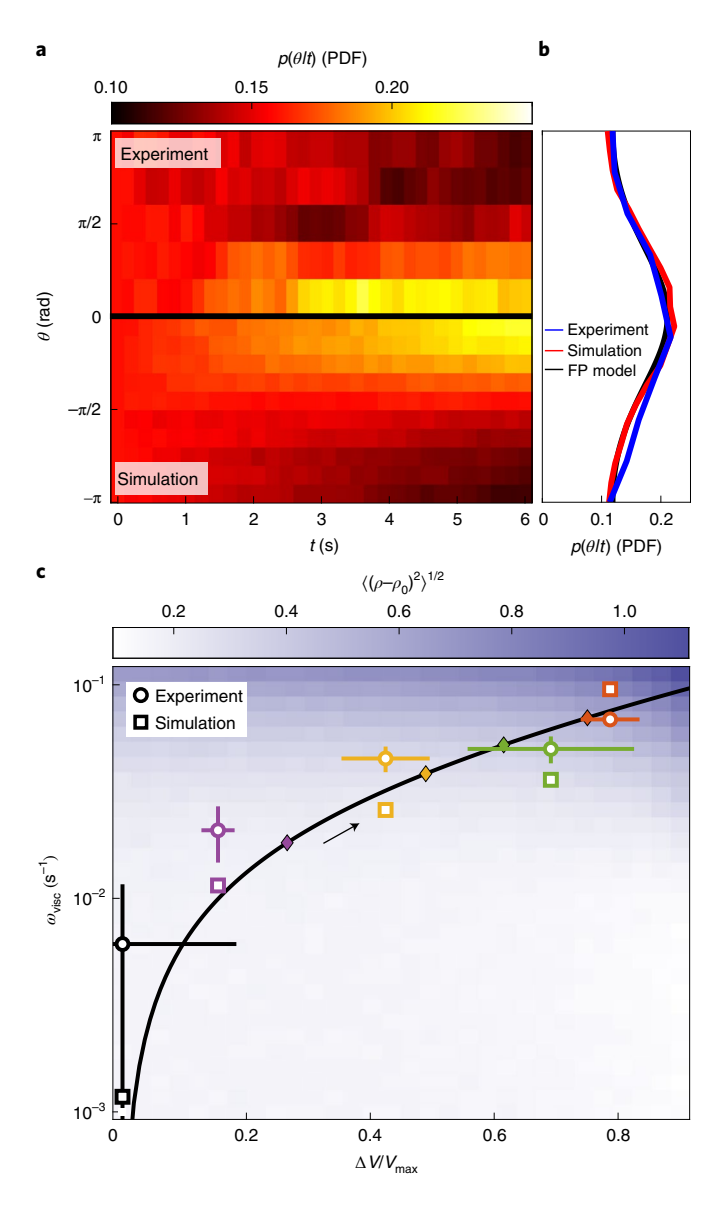


Fig. 3 | Simulations illustrate the competition between viscophobic drift and viscous slowdown driving cell accumulation. a, Time evolution of the conditional probability density of cell orientation (for $\nabla \eta = 7.2 \times 10^{-3} \text{ cP} \, \mu\text{m}^{-1}$) in experiments (top) and Langevin simulations (bottom), showing condensation of cell alignment down the viscosity gradient (Extended Data Fig. 6). Experimental cell tracks were selected from $400 \le x \le 600 \,\mu\text{m}$. **b**, Orientation distribution at t = 6 s from experiments and Langevin simulations in a agree with a Fokker-Planck (FP) model (Supplementary Section 5.3). c, The r.m.s. difference (colour scale; Methods) of cell densities between Langevin simulations (ρ) and theory without viscophobic turning (ρ_0) (Supplementary Section 4.1 and Extended Data Fig. 7). Squares are the best-match density profiles from simulations with circles representing experiments (marker colours correspond to experiments in Fig. 1i). The horizontal and vertical error bars for the circles were propagated from Fig. 1h and Fig. 2d, respectively. The black curve is the empirical scaling law (Supplementary Section 5.2) and the arrow indicates increasing $\nabla \eta$; diamonds correspond to experimental conditions (Fig. 1).

Although viscophobic turning seems to be rooted in the complexity of swimmer hydrodynamics, it results in strikingly simple reorientation dynamics that comprise a broader, universal class of motilities. The time evolution of the measured cell orientation

distribution, $p(\theta|t)$, illustrates the condensation of the cell swimming direction down the viscosity gradient (Fig. 3a, top and Extended Data Fig. 6). Similar to most microbes, the random walk nature of *C. reinhardtii* motility stems from noise in their orientation³³, modelled as rotational diffusion superimposed on the deterministic viscophobic turning:

$$\dot{\theta} = -\omega_{\text{visc}}\sin(\theta) + \sqrt{2D_{\text{r}}}\xi(t),\tag{1}$$

where the overdot indicates a time derivative, and ξ is Gaussian noise. A Langevin simulation (Methods) accurately reproduces the time evolution of cell orientation (bottom of Fig. 3a and Extended Data Fig. 6), which forms a well-defined peak after several seconds (Fig. 3b). Our observations of viscotactic turning are thus consistent with deterministic responses that underlie most eukaryotic systems³⁸ as opposed to the stochastic navigation of bacteria¹⁵. Importantly, viscotaxis seems to share universal dynamics that underpin a host of microbial responses to their physical environments—including gravitaxis^{17,18} and magnetotaxis^{19,39}—which are governed by a sinusoidal, paramagnetic-like torque in response to an external field. However, viscophobic reorientation is distinctive in that self-propulsion is fundamental to the cell response.

To elucidate the relative contributions of viscophobic turning versus viscous slowdown to cell transport, we employed a simplified, two-dimensional Langevin model. The simulated cell orientational dynamics are set by equation (1), and the translational dynamics are given by $\dot{x} = V(x)\cos(\theta)$ and $\dot{y} = V(x)\sin(\theta)$ (Supplementary Section 5.1). The essential features of the viscosity dependence are captured by a spatially varying (linear) cell swimming speed profile, V(x), which is parameterized by the speed difference across the channel normalized by the maximal speed in the low-viscosity zone $\Delta V/V_{\text{max}}$. The resulting Langevin simulations (Fig. 1i, dashed coloured lines) that best match the experimental cell density profiles faithfully reproduce the measured viscophobic turning rates (Fig. 3c, squares). The simulations also agree well with an empirical scaling law (Fig. 3c, black curve; Supplementary Section 5.2) based on the viscosity-dependent swimming speed (Fig. 1f) and turning rate (Fig. 2d).

Although viscophobic reorientation (Fig. 2d) and viscous slowdown (Fig. 1h) are intrinsically linked in experiments through the viscosity profile, simulations allowed us to untangle these effects by independently varying $\omega_{ ext{visc}}$ and $\Delta V/V_{ ext{max}}$. Density profiles from Langevin simulations (Fig. 1i, dashed), $\rho(x)$, and from theory based solely on the viscous slowdown, $\rho_0(x)$, were compared by examining the root mean squared (r.m.s.) density difference, $\langle (\rho - \rho_0)^2 \rangle^{1/2}$ (Fig. 3c, colour map and Extended Data Fig. 7). The sharp increase in r.m.s. density difference with increasing ω_{visc} is indicative of the progressive skewing of the cell density towards the low-viscosity region (Extended Data Fig. 7). For a fixed ω_{visc} , viscous slowdown causes cell accumulation on the viscous side, yet viscophobic motility moderates this trend more efficiently as the swimming speed contrast is increased. In real systems, the simultaneous increase of $\omega_{\rm visc}$ and $\Delta V/V_{\rm max}$ (Fig. 3c, black arrow) indicates that viscophobicity dominates for large viscosity gradients. The growing influence of viscophobic motility with increasing gradient presents an ecologically valuable asset for the escape or repulsion of cells from viscous environments1,2,5.

Our work illustrates an important transport mechanism for microalgae stemming from the competition between viscophobic turning and viscous slowdown, which we anticipate will have a rich dependency on organism flagellation. The short-flagella mutant experiments and the three-point force model show that negative viscotaxis is associated with the dominance of a flagellar thrust imbalance over any cell body drag imbalance in the gradient. Extending the model suggests that swimmers whose flagellar appendages are directly in line with the cell body—including many bacteria, such as

those probed in early experimental work^{6,7}—would exhibit positive viscotactic turning. This prediction remains to be experimentally demonstrated, but such positive viscotactic turning would exhibit a cooperative effect with viscous slowdown and exacerbate swimmer accumulation in high-viscosity regions. Although the observed viscophobic turning kinematics seem to be highly consistent with the proposed hydrodynamic mechanism, our work does not entirely rule out the potential for mechanosensing. Complementary studies at the level of single flagella will also be required to fully elucidate the potential impact of viscosity gradients on flagellar beat patterns and coordination^{26,33,34}. The demonstration of viscophobic turning has the potential to refine our understanding of cell motility in complex microbiological systems, where the impact of viscosity gradients on cell motility have been widely overlooked, ranging from biofilms⁴ to protective mucus layers^{2,3} to endangered coral ecosystems1. The experimental and analytical approaches established in this work will pave the way to understanding the manifestation of viscophobic motility in a range of important microorganisms and in complex fluid rheologies.

Online content

Any methods, additional references, Nature Research reporting summaries, source data, extended data, supplementary information, acknowledgements, peer review information; details of author contributions and competing interests; and statements of data and code availability are available at https://doi.org/10.1038/s41567-021-01247-7.

Received: 11 November 2020; Accepted: 9 April 2021; Published online: 27 May 2021

References

- Wild, C. et al. Coral mucus functions as an energy carrier and particle trap in the reef ecosystem. Nature 428, 66–70 (2004).
- Wheeler, K. M. et al. Mucin glycans attenuate the virulence of *Pseudomonas aeruginosa* in infection. *Nat. Microbiol.* 4, 2146–2154 (2019).
- 3. Suarez, S. S. & Pacey, A. A. Sperm transport in the female reproductive tract. *Hum. Reprod. Update* **12**, 23–37 (2006).
- Hall-Stoodley, L., Costerton, J. W. & Stoodley, P. Bacterial biofilms: from the natural environment to infectious diseases. *Nat. Rev. Microbiol.* 2, 95–108 (2004).
- Swidsinski, A. et al. Viscosity gradient within the mucus layer determines the mucosal barrier function and the spatial organization of the intestinal microbiota. *Inflamm. Bowel Dis.* 13, 963–970 (2007).
- Petrino, M. G. & Doetsch, R. N. 'Viscotaxis', a new behavioural response of Leptospira interrogans (biflexa) Strain b16. J. Gen. Microbiol. 109, 113–117 (1978).
- Daniels, M. J., Longland, J. M. & Gilbart, J. Aspects of motility and chemotaxis in spiroplasmas. J. Gen. Microbiol. 118, 429–436 (1980).
- Sherman, M. Y., Timkina, E. & Glagolev, A. Viscosity taxis in Escherichia coli. FEMS Microbiol. Lett. 13, 137–140 (1982).
- Schnitzer, M. J. Theory of continuum random walks and application to chemotaxis. Phys. Rev. E 48, 2553–2568 (1993).
- 10. Frangipane, G. et al. Dynamic density shaping of photokinetic E. coli. elife 7, e36608 (2018).
- Liebchen, B., Monderkamp, P., Ten Hagen, B. & Löwen, H. Viscotaxis: microswimmer navigation in viscosity gradients. *Phys. Rev. Lett.* 120, 208002 (2018)
- Datt, C. & Elfring, G. J. Active particles in viscosity gradients. *Phys. Rev. Lett.* 123, 158006 (2019).

- 13. Stocker, R. Marine microbes see a sea of gradients. *Science* **338**, 628–633 (2012).
- 14. Cavicchioli, R. et al. Scientists' warning to humanity: microorganisms and climate change. *Nat. Rev. Microbiol.* 17, 569–586 (2019).
- Berg, H. C. & Brown, D. A. Chemotaxis in *Escherichia coli* analysed by three-dimensional tracking. *Nature* 239, 500–504 (1972).
- Jékely, G. et al. Mechanism of phototaxis in marine zooplankton. Nature 456, 395–399 (2008).
- Durham, W. M., Kessler, J. O. & Stocker, R. Disruption of vertical motility by shear triggers formation of thin phytoplankton layers. *Science* 323, 1067–1070 (2009).
- Sengupta, A., Carrara, F. & Stocker, R. Phytoplankton can actively diversify their migration strategy in response to turbulent cues. *Nature* 543, 555–558 (2017)
- 19. Blakemore, R. P. Magnetotactic bacteria. Science 190, 377-379 (1975).
- Guadayol, Ö. et al. Microrheology reveals microscale viscosity gradients in planktonic systems. Proc. Natl Acad. Sci. USA 118, e2011389118 (2021).
- Lai, S. K., Wang, Y. Y., Wirtz, D. & Hanes, J. Micro- and macrorheology of mucus. Adv. Drug Deliv. Rev. 61, 86–100 (2009).
- Jatkar, A. A. et al. Measuring mucus thickness in reef corals using a technique devised for vertebrate applications. *Mar. Biol.* 157, 261–267 (2010).
- Atuma, C., Strugala, V., Allen, A. & Holm, L. The adherent gastrointestinal mucus gel layer: thickness and physical state in vivo. *Am. J. Physiol. Liver Physiol.* 280, G922–G929 (2001).
- Stabili, L., Schirosi, R., Parisi, M. G., Piraino, S. & Cammarata, M. The mucus of Actinia equina (Anthozoa, Cnidaria): an unexplored resource for potential applicative purposes. Mar. Drugs 13, 5276–5296 (2015).
- Cone, R. A. Barrier properties of mucus. Adv. Drug Deliv. Rev. 61, 75–85 (2009).
- Qin, B., Gopinath, A., Yang, J., Gollub, J. P. & Arratia, P. E. Flagellar kinematics and swimming of algal cells in viscoelastic fluids. Sci. Rep. 5, 9190 (2015).
- Martinez, V. A. et al. Flagellated bacterial motility in polymer solutions. Proc. Natl Acad. Sci. USA 111, 17771–17776 (2014).
- Shoele, K. & Eastham, P. S. Effects of nonuniform viscosity on ciliary locomotion. *Phys. Rev. Fluids* 3, 043101 (2018).
- Harris, E. H. The Chlamydomonas Sourcebook: Introduction to Chlamydomonas and its Laboratory Use Vol. 1 (Academic, 2009)
- 30. Goldstein, R. E. Green algae as model organisms for biological fluid dynamics. *Annu. Rev. Fluid Mech.* 47, 343–375 (2015).
- Kantsler, V., Dunkel, J., Polin, M. & Goldstein, R. E. Ciliary contact interactions dominate surface scattering of swimming eukaryotes. *Proc. Natl Acad. Sci. USA* 110, 1187–1192 (2013).
- Cates, M. E. Diffusive transport without detailed balance in motile bacteria: does microbiology need statistical physics? Rep. Prog. Phys. 75, 042601 (2012).
- Polin, M., Tuval, I., Drescher, K., Gollub, J. P. & Goldstein, R. E. Chlamydomonas swims with two gears in a eukaryotic version of run-and-tumble locomotion. Science 325, 487–490 (2009).
- Geyer, V. F., Jülicher, F., Howard, J. & Friedrich, B. M. Cell-body rocking is a dominant mechanism for flagellar synchronization in a swimming alga. *Proc.* Natl Acad. Sci. USA 110, 18058–18063 (2013).
- Lauga, E. & Powers, T. R. The hydrodynamics of swimming microorganisms. Rep. Prog. Phys. 72, 096601 (2009).
- Kuchka, M. R. & Jarvik, J. W. Short-flagella mutants of Chlamydomonas reinhardtii. Genetics 115, 685–691 (1987).
- 37. Oppenheimer, N., Navardi, S. & Stone, H. A. Motion of a hot particle in viscous fluids. *Phys. Rev. Fluids* 1, 014001 (2016).
- Waisbord, N. & Guasto, J. S. Peculiar polygonal paths. *Nat. Phys.* 14, 1161–1162 (2018).
- Rupprecht, J. F., Waisbord, N., Ybert, C., Cottin-Bizonne, C. & Bocquet, L. Velocity condensation for magnetotactic bacteria. *Phys. Rev. Lett.* 116, 168101 (2016).

Publisher's note Springer Nature remains neutral with regard to jurisdictional claims in published maps and institutional affiliations.

© The Author(s), under exclusive licence to Springer Nature Limited 2021

Methods

Cell culturing and media preparation. Wild-type (CC-1690 wild-type mt⁺, WT) and short-flagella mutants (CC-2347 shf1-277 mt⁻) of *C. reinhardtii* (Chlamydomonas Resource Center) were grown in 100 ml of minimal media (M1)⁴⁰ at 22 °C using gentle aeration and synchronized on a 14 h on and 10 h off light cycle. Cells were subcultured (10 ml) every 3 days at mid-exponential phase. Viscous media was prepared with PEO (molecular weight, 400,000 g mol⁻¹; Sigma-Aldrich) in M1 (Extended Data Table 2) at PEO concentrations of 0, 0.05, 0.10, 0.25, 0.50 and 0.82% (w/v), which remain Newtonian (overlap concentration $c^* \approx 3\%$ (w/v))^{41,42}. PEO solutions were mixed for 2 h at 40 r.p.m. (tube rotator; Fisherbrand) and 0.2% (w/v) bovine serum albumen was added to all solutions to reduce sticking to microchannel walls.

Microfluidics. Microfluidic devices were made using standard soft lithography techniques ¹³. Polydimethylsiloxane (Dow Corning SYLGARD 184) channels were cast on photoresist (Microchem) moulds fabricated via photolithography and plasma bonded to standard glass slides. Circular observation channels (diameter 5 mm; height 250 μ m) were used for bulk cell motility and microrheology measurements. Viscosity gradient generation channels (Fig. 1b) were designed with three inlets (width 0.5 mm) carrying a viscous PEO solution, cell suspension and M1 media, respectively. The three solutions were flow stratified for a minimum of 2 min using two syringe pumps (Harvard Apparatus), whereby flow rates were adjusted to maintain a 4:1:4 ratio of the stream widths (Supplementary Section 1). Upon halting the flow, a monotonic viscosity profile, $\eta(x)$, slowly evolved over 90 min (Extended Data Fig. 1) owing to the relatively low PEO diffusivity ¹⁴. The thin central band of *C. reinhardtii*, bracketed by fresh M1, ensured no chemotactic bias was introduced ²⁷ (Supplementary Section 3.2).

Microrheology and viscosity profile measurement. The viscosity of bulk Newtonian PEO solutions was measured through well-developed microrheology approaches⁴⁵ by seeding with dilute $(0.5 \,\mu l \,m l^{-1})$ tracer particles $(R = 0.25 \,\mu m; 2\%)$ solid; Life Technologies). Tracers were imaged using epifluorescence microscopy (×10 objective, 0.5 NA; Nikon Ti-e) and recorded (Blackfly S, FLIR Systems) at 4 $\,$ frames per second (fps) for 25 s. Mean square displacements of 488-1,153 particle trajectories, $\langle \Delta x^2 \rangle$, were measured over time Δt via particle tracking. A linear fit (Extended Data Fig. 4) of the mean square displacement $\langle \Delta x^2 \rangle = 2D\Delta t$ yielded the diffusivity, *D*, which was used to determine the viscosity from the Stokes–Einstein relation, $D = k_B T / 6\pi \eta R$ (where k_B is the Boltzmann constant and T the absolute temperature). Measured bulk viscosities (Extended Data Table 2) compared well with previously reported results⁴¹. Spatially resolved viscosity profiles $\eta(x)$ generated by the viscosity gradient assay (Fig. 1g) were measured using an identical approach to the bulk experiments, but particle tracks were partitioned into 11 equally spaced bins across the channel width (Extended Data Fig. 2). The time evolution of the viscosity profile was evaluated by acquiring video of fluorescent tracer motion (×10 objective, 0.2 NA) for 250 frames (63 s long) every 10 min for 90 min (Zyla, Andor Technology). The local viscosity was measured from the mean square displacement (Extended Data Fig. 2) in each spatially resolved bin over the 90 min experiment. Transient variations in viscosity rapidly decreased after 30 min (Extended Data Fig. 1). Thus, we analysed our primary quasi-steady viscotaxis assay results from 30-90 min after halting the flow, and we report the average viscosity profile over this time window (Fig. 1g). $\nabla \eta$ was calculated from a linear fit to the viscosity profile in the middle third of the microchannel. The viscosity gradient for each viscotaxis experiment is the average gradient within the $30-90\,\mathrm{min}$ interval (Extended Data Table 1). See Supplementary Section 2 for details.

Cell imaging and tracking. Imaging for viscotaxis experiments with C. reinhardtii was performed using phase-contrast microscopy (×10 objective, 0.2 NA; Nikon Ti-e). To ensure that phototactic effects did not bias cell motility measurements²⁹, experiments were performed in a darkened room equipped with blackout shades, a light shield was constructed to block stray light and the microscope's transmitted light source was equipped with a 665 nm long-pass filter (Thorlabs, Inc.), which is outside the spectral detection range of C. reinhardtii46. Control experiments in the absence of viscosity gradients (Extended Data Fig. 3) confirmed that no phototactic bias was present. Upon halting the flow and initializing the viscosity gradient formation, videos were recorded (Zyla, Andor Technology) for 1,000 frames each at 30 fps every 5 min for the first 90 min. Dilute cell suspensions (~66 cells per frame) ensured high-fidelity cell tracking and negligible cell-cell interactions⁴⁷ and mixing. Cells were tracked using a custom predictive particle tracking code written in MATLAB (2020b, MathWorks). Briefly, cell centroids were identified by intensity thresholding 48,49 and their trajectories were reconstructed via distance minimization of quadratic projections of cell motion in comparison with new candidate cell locations⁵⁰. Three or four replicate experiments were performed for each viscosity gradient for the experiments with WT cells and one to three replicates for the experiments with short-flagella mutant cells. Spatial cell density and swimming speed profiles were measured by partitioning the channel into 11 equally spaced bins (~90 μ m wide; Fig. 1h,i). To quantify ω as a function of orientation (Fig. 2), trajectories were smoothed with a Gaussian filter (1 s standard deviation) to remove high-frequency fluctuations stemming from the natural helical trajectories of C. reinhardtii⁵¹. Occasional stuck or non-motile cells were

removed from the data providing a minimum ratio of track contour length to radius of gyration of \geq 4 and 6 for the WT and short-flagella mutants, respectively.

Rotational cell diffusion. Rotational diffusion of WT *C. reinhardtii* was measured by recording cells (×2 objective, 0.1 NA; Blackfly S, FLIR Systems) for 10 min at 15 fps and 10 fps in bulk 0.996 cP and 4.48 cP media, respectively. Cell tracks with a minimum duration of 15 s were filtered as described above, and minimum mean cell swimming speeds of 54.2 $\mu m \, s^{-1}$ and 15.0 $\mu m \, s^{-1}$ were required for the 0.996 cP and 4.48 cP media, respectively. The mean square displacements (Extended Data Fig. 5) were fitted (Extended Data Fig. 5, solid lines) using the analytical result⁵² $\langle \Delta r^2 \rangle = 0.5 V^2/D_r^2 (2D_r t + \exp(-2D_r t) - 1)$, where the 2D projections of the cells' 3D random walks accurately captured the amplitude of their effective in-plane

3D random walks accurately captured the amplitude of their effective in-plane rotational noise⁵³. For measured mean swimming speeds $V=74.7~\mu \rm m~s^{-1}$ and $22.7~\mu \rm m~s^{-1}$, the resulting rotational diffusion coefficients were $D_{\rm r}=0.070~\rm s^{-1}$ and $0.068~\rm s^{-1}$ for $0.996~\rm cP$ and $4.48~\rm cP$, respectively.

Langevin simulation parameters. Langevin simulations (Fig. 3 and Extended Data Figs. 6 and 7) were performed by numerically integrating the equations of motion for cell position and orientation using a fourth-order Runge-Kutta method with a time step of 0.001 s (Supplementary Section 5.1). Swimmers were uniformly seeded across the domain with random orientation, including 500 swimmers for Fig. 3c and Extended Data Fig. 7 and 100,000 for Fig. 3a,b and Extended Data Fig. 6, which were integrated for 1,000 s and 6 s, respectively. On the basis of the measured cell motility parameters (Figs. 1 and 2), the viscophobic rotation rate and viscous slowdown were independently varied via $\omega_{
m visc}$ and $\Delta V/V_{\text{max}}$, respectively. Typical constant values were chosen for all simulations (Fig. 3 and Extended Data Figs. 6 and 7), including $V_{\rm max} = 100 \, \mu \rm m \, s^{-1}$ and $D_{\rm r} = 0.069 \, s^{-1}$ Two-dimensional Langevin simulations using $D_{\rm r}$ measured from 2D projections of cell trajectories (see above) have been shown to accurately reproduce measured cell transport properties^{53,54}. Cell scattering from the microchannel side walls was quantified³¹ from control experiments $(\nabla \eta = 0 \text{ cP} \mu \text{m}^{-1})$ and implemented as an empirical boundary condition (Supplementary Section 5.1). A total of 900 simulations spanning $\Delta V/V_{\rm max}$ and $\omega_{\rm visc}$ were performed for Fig. 3c. For a fixed $\Delta V/V_{\text{max}}$ (corresponding to a $\nabla \eta$), the minimum r.m.s. difference between experimental (Fig. 1i, solid lines) and simulated (Extended Data Fig. 7) density profiles determined the best match $\omega_{\mbox{\tiny visc}}$ from simulations (Fig. 3c, squares), which compared well with measured values (Fig. 3c, circles).

Reporting Summary. Further information on research design is available in the Nature Research Reporting Summary linked to this article.

Data availability

Data files used during the current study are publicly available at https://doi.org/10.7910/DVN/QXI6X1. Source data are provided with this paper.

Code availability

The algorithms and simulation codes are described in the Methods and Supplementary Information. Code to reproduce the analysis reported is publicly available at https://doi.org/10.7910/DVN/QXI6X1.

References

- Sager, R. & Granick, S. Nutritional studies with Chlamydomonas reinhardi. Ann. NY Acad. Sci. 56, 831–838 (1953).
- Ebagninin, K. W., Benchabane, A. & Bekkour, K. Rheological characterization of poly(ethylene oxide) solutions of different molecular weights. *J. Colloid Interf. Sci.* 336, 360–367 (2009).
- 42. Grigorescu, G. & Kulicke, W.-M. Prediction of Viscoelastic Properties and Shear Stability of Polymers in Solution (Springer, 2000).
- Xia, Y. & Whitesides, G. M. Soft lithography. Annu. Rev. Mater. Sci. 28, 153–184 (1998).
- Devanand, K. & Selser, J. C. Polyethylene oxide does not necessarily aggregate in water. *Nature* 343, 739–741 (1990).
- Waigh, T. A. Microrheology of complex fluids. Rep. Prog. Phys. 68, 685–742 (2005).
- Kreis, C. T., Le Blay, M., Linne, C., Makowski, M. M. & Bäumchen, O. Adhesion of *Chlamydomonas* microalgae to surfaces is switchable by light. *Nat. Phys.* 14, 45–49 (2018).
- Rafaï, S., Jibuti, L. & Peyla, P. Effective viscosity of microswimmer suspensions. *Phys. Rev. Lett.* 104, 098102 (2010).
- Cheezum, M. K., Walker, W. F. & Guilford, W. H. Quantitative comparison of algorithms for tracking single fluorescent particles. *Biophys. J.* 81, 2378–2388 (2001)
- Crocker, J. C. & Grier, D. G. Methods of digital video microscopy for colloidal studies. J. Colloid Interf. Sci. 179, 298–310 (1996).
- Ouellette, N. T., Xu, H. & Bodenschatz, E. A quantitative study of three-dimensional Lagrangian particle tracking algorithms. *Exp. Fluids* 40, 301–313 (2006).

- Crenshaw, H. C. A new look at locomotion in microorganisms: rotating and translating. Am. Zool. 36, 608–618 (1996).
- 52. Howse, J. R. et al. Self-motile colloidal particles: from directed propulsion to random walk. *Phys. Rev. Lett.* **99**, 48102 (2007).
- Rusconi, R., Guasto, J. S. & Stocker, R. Bacterial transport suppressed by fluid shear. Nat. Phys. 10, 212–217 (2014).
- Dehkharghani, A., Waisbord, N., Dunkel, J. & Guasto, J. S. Bacterial scattering in microfluidic crystal flows reveals giant active Taylor–Aris dispersion. *Proc. Natl Acad. Sci. USA* 116, 11119–11124 (2019).
- 55. Korson, L., Drost-Hansen, W. & Millero, F. J. Viscosity of water at various temperatures. *J. Phys. Chem.* **73**, 34–39 (1969).

Acknowledgements

We thank G. J. Elfring for helpful discussions and R. J. Henshaw for comments on the manuscript. This work was funded by NSF awards CAREER-1554095 and CBET-1701392 to J.S.G.

Author contributions

M.R.S., N.W. and J.S.G. designed the research. M.R.S. and N.W. performed experiments, and M.R.S., N.W. and D.M.W. analysed experimental data. All authors contributed to simulations and theoretical analyses and wrote the paper.

Competing interests

The authors declare no competing interests.

Additional information

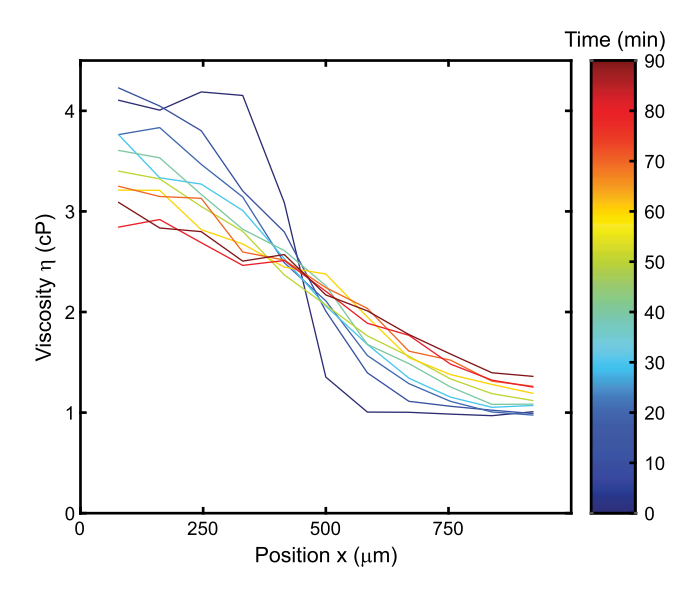
Extended data is available for this paper at https://doi.org/10.1038/s41567-021-01247-7.

Supplementary information The online version contains supplementary material available at https://doi.org/10.1038/s41567-021-01247-7.

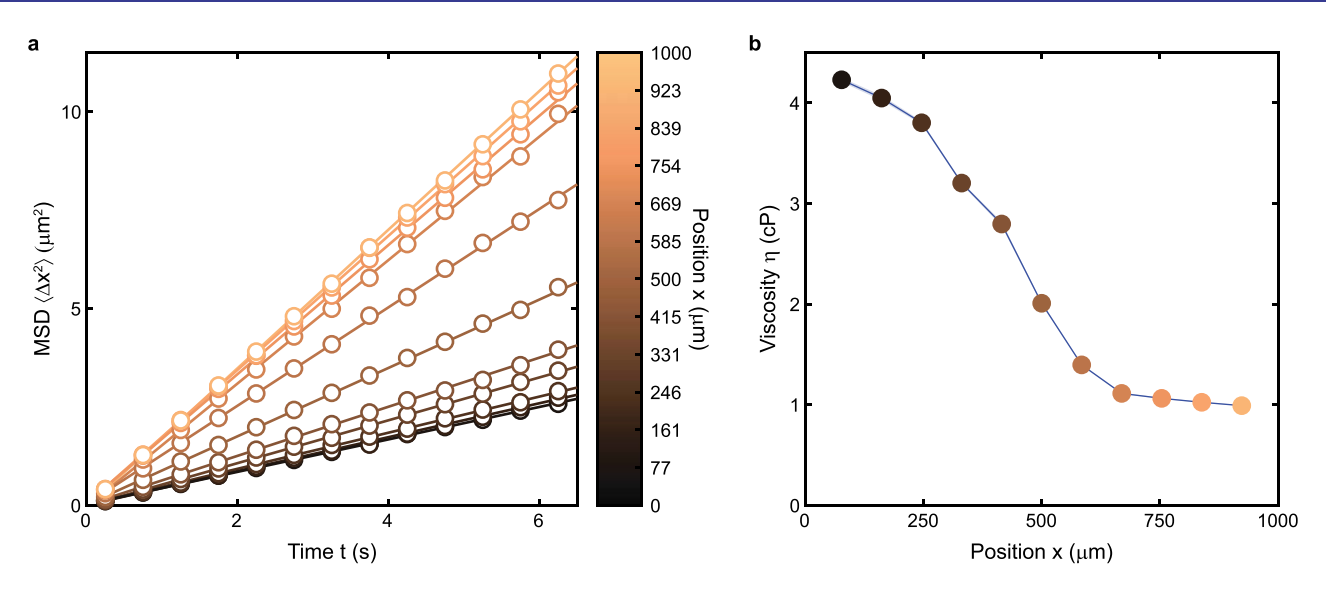
Correspondence and requests for materials should be addressed to J.S.G.

Peer review information *Nature Physics* thanks Arnold Mathijssen and the other, anonymous, reviewer(s) for their contribution to the peer review of this work.

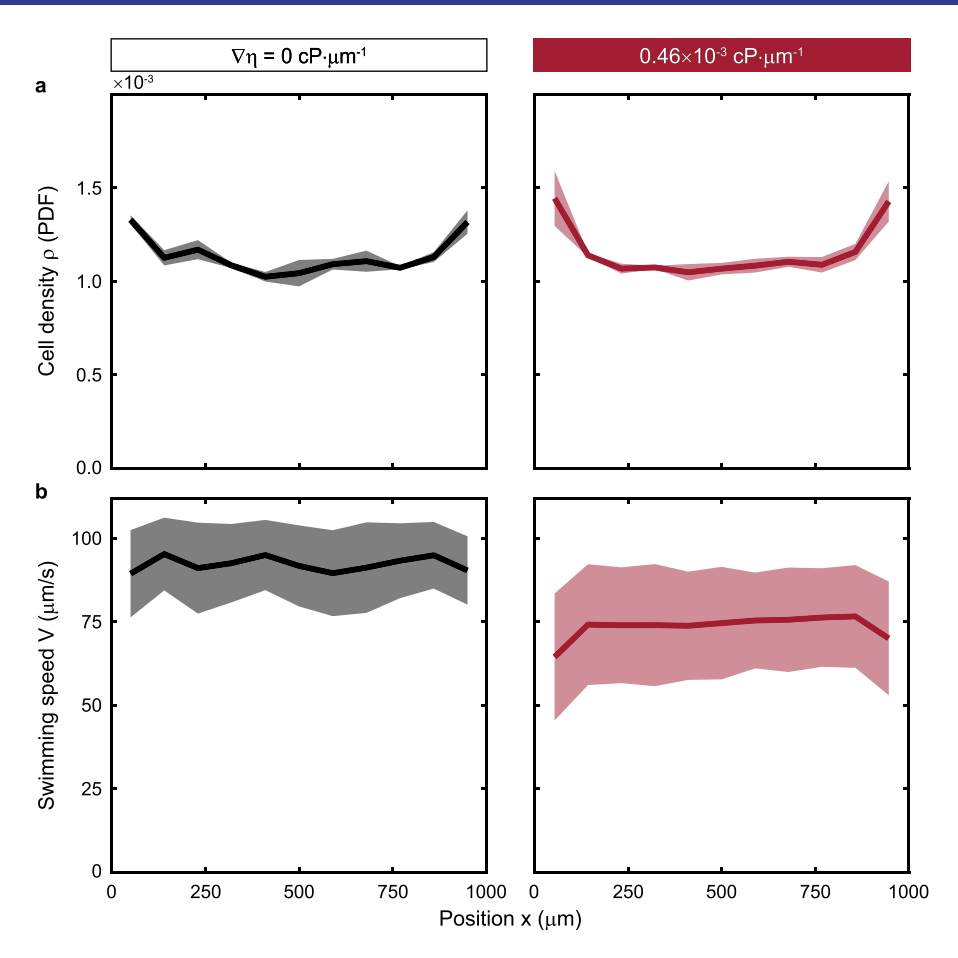
Reprints and permissions information is available at www.nature.com/reprints.



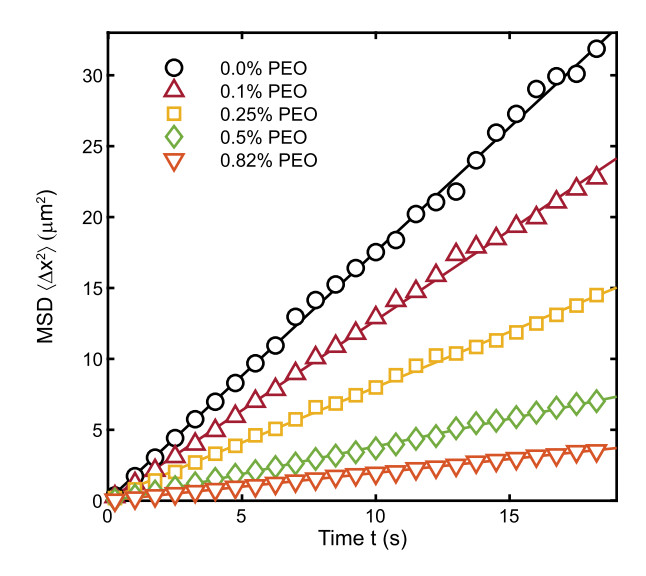
Extended Data Fig. 1 | Time evolution of the viscosity profile. Transient diffusion of the PEO molecules results in a viscosity profile that evolves from a near step function to a smooth monotonic profile. Swimming cell assays are analyzed in the time range $30 \le t \le 90$ min, when the gradient evolves more slowly, and the profile is approximately linear in the center of the channel. The slope of the viscosity profile is quantified by fitting a line to the five central points in the channel. The reported viscosity gradient, $\nabla \eta$, is the average slope of the viscosity profiles from 30-90 min (Extended Data Table 1).



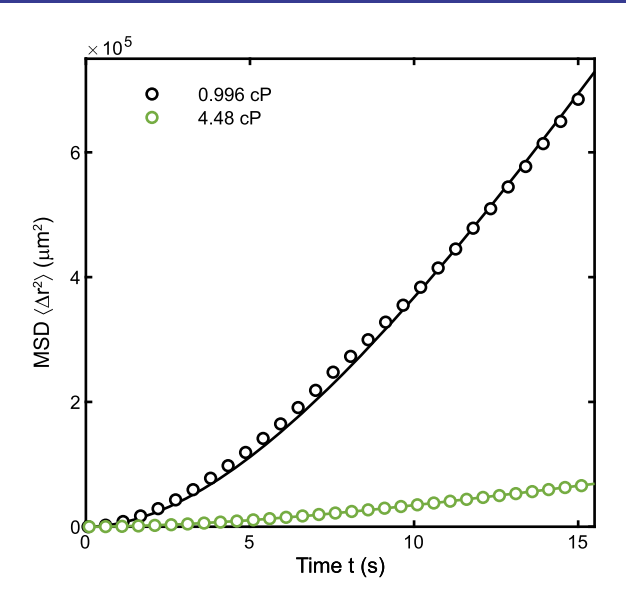
Extended Data Fig. 2 | Spatially resolved microrheology quantifies the viscosity profile in a microfluidic device. a, The mean square displacement (MSD) of tracer particles in different locations across the microfluidic viscosity gradient device at time, t = 10 min ($\nabla \eta = 3.4 \times 10^{-3} \, cP \cdot \mu \text{m}^{-1}$; see also Extended Data Fig. 1). Solid lines are linear fits to the MSDs. **b**, The slopes of the tracer particle MSDs in **a** are used to determine the spatially resolved viscosity profile, $\eta(x)$, across 11 bins of the microchannel width using Stokes-Einstein relation (Supplementary Section 2.2). Shaded region (smaller than the markers) represents the propagation of uncertainty from the error of the fit in **a**.



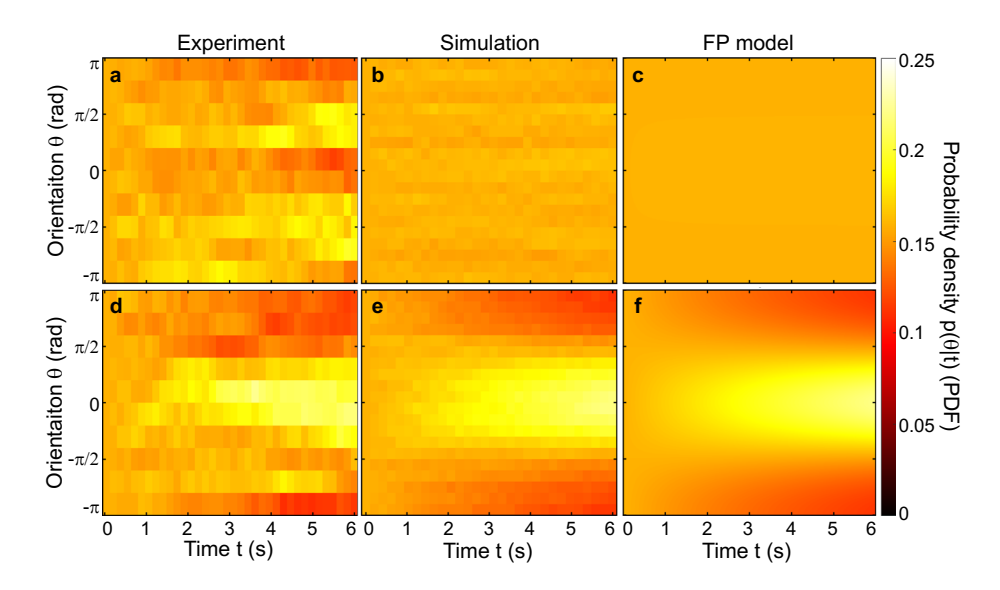
Extended Data Fig. 3 | Control experiments show negligible chemotaxis and chemokinetic effects for wild-type *C. reinhardtii* in PEO gradients. a,b, Viscotaxis assays reveal the local, measured cell density (a) and mean swimming speed (b) remain spatially uniform for small viscosity gradients. Base PEO concentrations of 0.05% in viscous media inlet ($\nabla \eta = 0.46 \times 10^{-3} \, cP \cdot \mu m^{-1}$; N=3; right) are comparable to the control experiment with no viscosity gradient ($\nabla \eta = 0.cP \cdot \mu m^{-1}$; N=4; left, repeated from Fig. 1h,i). For these control experiments, the base PEO concentration (0.05%) is nearly the same order of magnitude as the maximum gradient (0.82%), yet has no appreciable effect on the local viscosity. Thus, the lack of discernible cell accumulation and the lack of statistically significant spatial variations in swimming speed indicate that PEO likely does not act as a chemoattractant nor does it have any chemokinetic effect on *C. reinhardtii*. The shaded areas represent the standard error.



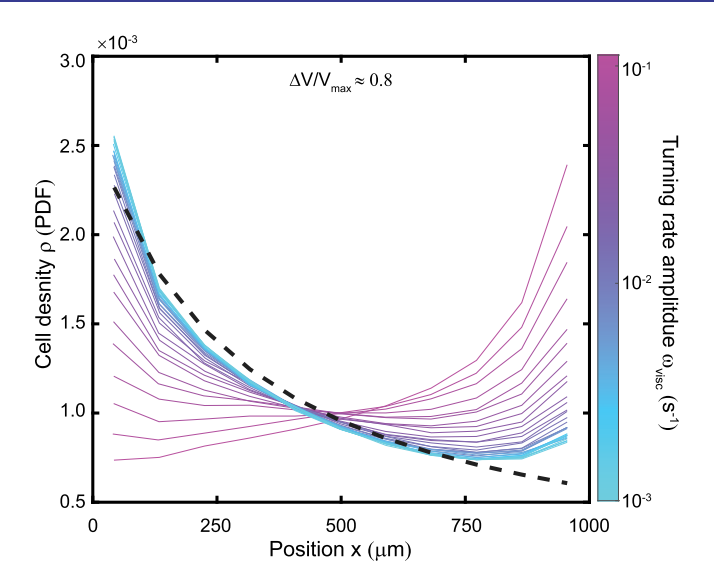
Extended Data Fig. 4 | Mean square displacements of tracer particles for viscosity measurements in bulk fluid. Microrheology quantifies the viscosity of PEO solutions in M1 media at various concentrations. The slopes of linear fits (solid lines) to the mean square displacements (MSDs; markers) yield the tracer particle diffusion coefficients, which are used to determine the viscosity of the solution via the Stokes-Einstein relation (Supplementary Section 2.1). Measured viscosities are listed in Extended Data Table 2.



Extended Data Fig. 5 | Measurement of mean square displacement (MSD) of wild-type C. reinhardtii in uniform viscosity to determine rotational diffusion coefficient. Mean square displacements of C. reinhardtii were measured in 0.996 cP (\approx 1,800 trajectories) and 4.48 cP (\approx 10,700 trajectories) bulk viscosities. The resulting MSDs were fitted using an analytical result for a persistent random walk 52,53 , $\langle \Delta r^2 \rangle = 0.5 \ V^2/D_t^2 (2D_t t + \exp(-2D_t t) - 1)$, where the ensemble averaged cell swimming speeds, V, are known independently (74.7 μ m/s and 22.7 μ m/s, respectively), and the rotational diffusion coefficient, D_r is the lone fitting parameter. The resulting rotational diffusion coefficients were $D_r = 0.070 \ s^{-1}$ and $0.068 \ s^{-1}$. As a sensitivity analysis, varying the fit window from 10 s to 20 s resulted in $D_r = 0.071 \pm 0.006 \ s^{-1}$ and $0.068 \pm 0.001 \ s^{-1}$ for $0.996 \ cP$ and $4.48 \ cP$, respectively, where the error is the standard deviation of the resulting rotational diffusion coefficients.



Extended Data Fig. 6 | Time evolution of swimming cell orientation distribution in a viscosity gradient. a-c, In the absence of a viscosity gradient or viscophobic turning, an initially random uniform distribution of cell swimming orientations remains random, as illustrated across experiments, Langevin simulations, and a Fokker-Plank (FP) model, respectively. **d-f**, In contrast, in the presence of a viscosity gradient or orientation dependent viscophobic turning rate, the orientation of cells readily condenses in the down-gradient direction. Experimentally measured cell swimming trajectories were sub-sampled from the central portion $(400\mu\text{m} \le x \le 600\mu\text{m})$ of the microfluidic gradient generating channel with a uniform orientation distribution $p(\theta|t)$ at t=0 for $\nabla \eta=0$ cP· μ m⁻¹ (**a**; control, \approx 1,170 trajectories) and for $\nabla \eta=7.2\times10^{-3}$ cP· μ m⁻¹ (**d**; \approx 1,330 trajectories). Peaks in **a** at \approx 6 s are due to cell collisions with microchannel walls. Langevin simulations in the absence (**b**) and presence (**e**) of viscophobic turning ($\omega_{\text{visc}}=0.07\text{ s}^{-1}$, $\Delta V/V_{\text{max}}=0.776$) show quantitative agreement with experiments having matching conditions (Extended Data Fig. 7 and Fig. 3a,b) in **a** and **d**, respectively. A one-dimensional Fokker-Planck model of the cell swimming orientation distribution (Supplementary Section 5.3) likewise captures the time evolution of the conditional probability density for the control (**c**) and corresponding maximum viscosity gradient conditions (**f**; Fig. 3b).



Extended Data Fig. 7 | Comparison of cell density profile due to (viscous) slowdown and Langevin simulations incorporating viscophobic turning. Langevin simulations enable independent exploration of the parameters $\Delta V/V_{max}$ and ω_{visc} , and include an empirical wall scattering boundary condition (Supplementary Section 5.1). Cell density profiles, $\rho(x)$, are shown for fixed $\Delta V/V_{max}$ and a range of turning rate amplitudes (solid lines). The resulting density profiles are compared to a theoretical distribution, ρ_0 , for cells with spatially varying swimming speed in the absence of viscophobic turning (black dashed curve; Supplementary Section 4.1).

Extended Data Table 1 | Measured viscosity gradients for viscotaxis experiments

PEO concentration in "viscous media" inlet |Measured viscosity gradient, $\nabla \eta$

$(\mathrm{w/v})$	$(\mathbf{cP}{\cdot}\mu\mathbf{m}^{-1})$
0.0%	0
0.05%	0.46×10^{-3} †
0.1%	$0.79 \times 10^{-3} \pm 0.75 \times 10^{-4}$
0.25%	$2.2 \times 10^{-3} \pm 3.41 \times 10^{-4}$
0.5%	$3.4 \times 10^{-3} \pm 9.60 \times 10^{-4}$
0.82%	$7.2 \times 10^{-3} \pm 1.9 \times 10^{-3}$

Viscosity gradients, $\nabla \eta$, for each of the tested gradient conditions were generated by controlling the bulk PEO concentration/viscosity in the viscous media inlet (Fig. 1b). Viscosity gradients were measured by fitting a line to the measured viscosity profiles in the central third of the channel. The slopes of the fits were then averaged to determine the mean $\nabla \eta$ over the experiment time window of 30-90 min. The \dagger indicates interpolation by quadratic fit. Uncertainty represents the standard deviation of the fitted viscosity profile slopes from 30-90 min (Extended Data Fig. 1).

Extended Data Table 2 | Viscosity of bulk PEO solutions

PEO Concentration (w/v)	Viscosity (cP)	Viscosity (cP)	
	[Ebagninin et al. ⁴¹]	[current study]	
0.0%	1*	0.996 ± 0.0052	
0.05%	1.09^{\dagger}	=	
0.1%	1.36^{\dagger}	1.38 ± 0.0071	
0.125%	1.51^{\dagger}	-	
0.25%	2	2.23 ± 0.0121	
0.375%	3.44^{\dagger}	-	
0.5%	5	4.48 ± 0.0195	
0.82%	9.01 †	8.96 ± 0.0264	
1.0%	12	-	

The dynamic viscosities of aqueous PEO solutions of various concentrations reported in the literature of compared to the present study in M1 media (measured by microrheology; \approx 22°C). The * indicates the known viscosity value at 20°C and the † indicates a quadratic interpolation of Ebagninin et al.4. Experimental uncertainty represents the propagation of error from the calculation of the diffusion coefficient.

Extended Data Table 3 | Measured transient viscosity gradient for viscotaxis experiments

	Measured viscosity gradient:	
(min)	$ \boxed{ \mathbf{0.5\%} \ \mathbf{PEO} \ \nabla \eta(t) \ (\mathbf{cP} \cdot \mu \mathbf{m}^{-1}) } $	$igg \mathbf{0.82\%} \ \mathbf{PEO} \ igtriangledown \nabla \eta(t) \ (\mathbf{cP} \cdot \mu \mathbf{m}^{-1})$
10	6.6×10^{-3}	15.1×10^{-3}
20	5.5×10^{-3}	12.3×10^{-3}
30	4.9×10^{-3}	10.1×10^{-3}
40	4.3×10^{-3}	9.4×10^{-3}
50	3.6×10^{-3}	7.5×10^{-3}
60	3.3×10^{-3}	6.9×10^{-3}

Viscosity gradients were measured by fitting a line to the measured viscosity profiles in the central third of the channel. The slopes of the fits determine the unsteady viscosity gradient, $\nabla \eta(t)$, at early times in the assay as the PEO molecules diffuse across the microfluidic device. 0.5% and 0.82% PEO transient viscosity gradient data correspond to steady experiments (30-90 min post flow) for $\nabla \eta = 3.4 \times 10^{-3} \, \text{cP} \cdot \mu \text{m}^{-1}$ and $\nabla \eta = 7.2 \times 10^{-3} \, \text{cP} \cdot \mu \text{m}^{-1}$ (green and orange in Fig. 1), respectively.

nature research

Corresponding author(s):	Jeffrey S. Guasto	
Last updated by author(s):	Feb 11, 2021	

Reporting Summary

Nature Research wishes to improve the reproducibility of the work that we publish. This form provides structure for consistency and transparency in reporting. For further information on Nature Research policies, see our <u>Editorial Policies</u> and the <u>Editorial Policy Checklist</u>.

_				
C	ta:	tic	٠±١.	\sim

For	all statistical an	alyses, confirm that the following items are present in the figure legend, table legend, main text, or Methods section.		
n/a	Confirmed			
	The exact	sample size (n) for each experimental group/condition, given as a discrete number and unit of measurement		
	A stateme	ent on whether measurements were taken from distinct samples or whether the same sample was measured repeatedly		
\boxtimes		tical test(s) used AND whether they are one- or two-sided non tests should be described solely by name; describe more complex techniques in the Methods section.		
\boxtimes	A descript	cion of all covariates tested		
\boxtimes	A descript	cion of any assumptions or corrections, such as tests of normality and adjustment for multiple comparisons		
	A full description of the statistical parameters including central tendency (e.g. means) or other basic estimates (e.g. regression coefficient) AND variation (e.g. standard deviation) or associated estimates of uncertainty (e.g. confidence intervals)			
\boxtimes	For null hypothesis testing, the test statistic (e.g. <i>F</i> , <i>t</i> , <i>r</i>) with confidence intervals, effect sizes, degrees of freedom and <i>P</i> value noted Give <i>P</i> values as exact values whenever suitable.			
\boxtimes	For Bayesian analysis, information on the choice of priors and Markov chain Monte Carlo settings			
\boxtimes	For hierarchical and complex designs, identification of the appropriate level for tests and full reporting of outcomes			
\boxtimes	Estimates of effect sizes (e.g. Cohen's d , Pearson's r), indicating how they were calculated			
Our web collection on <u>statistics for biologists</u> contains articles on many of the points above.				
Software and code				
Poli	cy information	about <u>availability of computer code</u>		
Da	ata collection	Data were collected using commercially available Nikon NIS-Elements and Spinnaker SDK software.		
Da	ata analysis	Data analysis were performed using customized code written in MATLAB (MathWorks).		
For manuscripts utilizing custom algorithms or software that are central to the research but not yet described in published literature, software must be made available to editors and reviewers. We strongly encourage code deposition in a community repository (e.g. GitHub). See the Nature Research guidelines for submitting code & software for further information.				

Data

Policy information about availability of data

All manuscripts must include a data availability statement. This statement should provide the following information, where applicable:

- Accession codes, unique identifiers, or web links for publicly available datasets
- A list of figures that have associated raw data
- A description of any restrictions on data availability

The data and computer codes used in the current study are available from the corresponding author upon reasonable request.

making your selection.

Field-spec	ific reporting	
Please select the one b	pelow that is the best fit for your research	. If you are not sure, read the appropriate sections before
∑ Life sciences	Behavioural & social sciences	Ecological, evolutionary & environmental sciences
For a reference copy of the document with all sections, see nature.com/documents/nr-reporting-summary-flat.pdf		

Life sciences study design

All studies must disclose on these points even when the disclosure is negative.

Sample size

Sample size of wild-type cells consisted of N=3-4 biological replicates comprising approximately 2,100-9,200 individual cell trajectories per replicate shown in Fig. 1 and 3,454-7,730 subsampled trajectories per data point used in Fig. 2 and 3 (steady-state). Steady-state short-flagella mutant data consisted of N = 1-3 biological replicates comprising 792-3,859 trajectories per data point in Fig 2d. Transient gradient data consisted of 319-760 cell trajectories per data point for both wild-type and short-flagella cells in Fig 2d.

Data exclusions

No data were excluded from analyses. Trajectories of cells stuck to surfaces were identified and removed using a filtering parameter defined as the ratio of the contour length of the track divided by the radius of gyration (Methods). When calculating the rotational diffusion coefficient, cell tracks were required to also have a minimum length and a minimum mean cell swimming speed. See supplementary information for details.

Replication

All attempts at replication were self consistent, and experiments were replicated using cells grown from separate cultures. (See "Sample size" above for details)

Randomization

Randomization is not relevant to study. Samples were allocated randomly and measured on different days and experiments were performed trying to carefully reproduce the initial conditions to test repeatability.

Blinding

Blinding was not relevant to our study, as we were measuring microorganism motility using automated tracking codes.

Reporting for specific materials, systems and methods

We require information from authors about some types of materials, experimental systems and methods used in many studies. Here, indicate whether each material, system or method listed is relevant to your study. If you are not sure if a list item applies to your research, read the appropriate section before selecting a response.

Materials & experimental systems		Methods	
n/a	Involved in the study	n/a	Involved in the study
\boxtimes	Antibodies	\times	ChIP-seq
	Eukaryotic cell lines	\times	Flow cytometry
\boxtimes	Palaeontology and archaeology	\times	MRI-based neuroimaging
\boxtimes	Animals and other organisms		
\boxtimes	Human research participants		
\boxtimes	Clinical data		
\boxtimes	Dual use research of concern		

Eukaryotic cell lines

(See ICLAC register)

Policy information about cell lines

Cell line source(s)

Strains CC-1690 wild type mt+ [Sager 21 gr] and CC-2347 shf1-277 mt- of Chlamydomonas reinhardtii were obtained from the Chlamydomonas Resource Center at the University of Minnesota.

Authentication

Body size, length of flagella, and ensemble mean swimming speed were used to authenticate cell lines.

Cell lines were not tested for mycoplasma contamination.

Commonly misidentified lines

No commonly misidentified cell lines were used in this study.